Received: 25 March 2021 | Revised: 28 May 2021 | Accepted: 1 June 2021

DOI: 10.1111/ijac.13829

International Journal of Applied Ceramic TECHNOLOGY

SPECIAL ISSUE ARTICLE

Crystalline ytterbium disilicate environmental barrier coatings made by high velocity oxygen fuel spraying

Markus Wolf[1,2] | **Daniel Emil Mack**[1] | **Georg Mauer**[1] | **Olivier Guillon**[1,3] | **Robert Vaßen**[1,2]

[1]Forschungszentrum Jülich GmbH, Institute of Energy and Climate Research, Materials Synthesis and Processing (IEK-1, Jülich, Germany

[2]Institut für Werkstoffe, Ruhr-Universität Bochum, Bochum, Germany

[3]Jülich Aachen Research Alliance: JARA-Energy, Jülich, Germany

Correspondence
Daniel Emil Mack, Forschungszentrum Jülich GmbH, Institute of Energy and Climate Research, Materials Synthesis and Processing (IEK-1), 52425 Jülich, Germany.
Email: d.e.mack@fz-juelich.de

Funding information
The authors acknowledge financial support from MTU Aero Engines AG under contract Z0609.21.18.

Abstract

Dense environmental barrier coatings (EBCs) are an essential prerequisite to exploit the advantages offered by SiC-based fiber reinforced ceramic matrix composites (CMCs) to increase efficiency in gas turbines. Today's state-of-the art materials for application as EBCs are rare-earth (RE) silicates which, however, form amorphous phases upon rapid quenching from the melt. This makes their processing by thermal spray a challenge. Recently, high velocity oxygen fuel (HVOF) spraying was proposed as potential solution since the melting degree of the feedstock can be controlled effectively. This work studies the deposition of ytterbium disilicate (YbDS) at short stand-off distances and variant total feed rates and oxy-fuel ratios of the working gas. It was found that the overall degree of crystallinity could be kept at high level above 90%. The kinetic energy transferred by impinging particles was found to be an effective parameter to control the densification of the coatings. Porosities well below 10% were achieved while fully dense coatings were impeded due to the progressive accumulation of stresses in the coatings.

KEYWORDS

ceramic, environmental barrier coating (EBC), high velocity oxygen fuel (HVOF), porosity, thermal spray

1 | INTRODUCTION

Dense environmental barrier coatings (EBCs) are an essential prerequisite for the exploitation of the advantages offered by SiC-based fiber reinforced ceramic matrix composites (CMCs) to increase efficiency in modern gas turbines. Thanks to their good mechanical high-temperature properties and low specific weight, the non-oxide SiC/SiC CMCs represent a promising alternative to temperature-limited metallic materials for modern gas turbines.[1–3] However, a particular problem with these CMCs is their high susceptibility to corrosion in atmospheres containing water vapor at temperatures above 1200°C. The formation and subsequent volatilization of the silicon oxide scale must be suppressed by protective coatings which are more stable against water vapor corrosion. They must be well adapted to the thermomechanical properties of the base materials.[4, 5]

Today's state-of-the art materials for application as EBCs for SiC-based CMCs are rare-earth (RE) silicates where the disilicates (DS) are best adapted to the thermomechanical properties of the SiC CMCs on the one hand, while on the other hand the monosilicates (MS) are superior in terms of corrosion resistance.[6] As for most of the RE-silicates for high temperature applications, the difficulty is to manufacture coatings which are pure, crystalline and gas tight. The reason is that the silicates are prone to solidify in the amorphous state when rapidly formed or quenched from high temperatures. In plasma spray, which is one of the most established technologies to manufacture high temperature coatings, this means that the silicate coatings are deposited predominantly in amorphous state. When these layers are exposed to high

temperatures, recrystallization leads to volume loss and formation of cracks, which reduces the mechanical integrity and gas tightness of the layers.

Nevertheless, the route via thermal spraying remains most attractive, due to simplicity and low costs. To avoid the problems caused by subsequent crystallization, attempts were made to achieve substantial crystallization already during coating deposition at least to a considerable amount. Various solutions have been proposed to achieve deposition conditions at substrate temperatures sufficiently high for crystallization, for example, in an oven[7] or under low-pressure conditions.[8]

In a recent work, Bakan et al.[9] demonstrated that YbDS coatings with porosities below 10% and relatively high crystallinity of more than 30% could be produced by high velocity oxygen fuel spraying (HVOF). This is in accordance to prior works where coatings from ceramic materials such as alumina, chromia, titania, or even hydroxyapatite with high degrees of crystallinity and high phase purity could be achieved by HVOF deposition starting from small-sized or nano-agglomerated feedstocks.[10–13] All studies concluded that dense ceramic coatings can be obtained with sufficient deposition efficiency only if particles are melted sufficiently so that good adhesion between the deposited splats is achieved, while crystallinity in the coating depends mainly on the amount of partially unmelted powder particles. Here, the HVOF process benefits from relatively low particle temperatures and high particle velocities which result from limited flame temperature and the supersonic jet in contrast to plasma spraying. The size of (primary) particles and the stand-off distance (SoD) were identified as major parameters affecting the degree of melting. While the SoD essentially determines the time of flight, the surface area to mass ratio is increased the smaller the particles are. This is particularly true for the nano-sized primary feedstock particles of agglomerated feedstocks. Both characteristics have major impact to the integral heat transfer along the trajectory.

More specifically, Bakan et al. utilized high total gas feeds to achieve high-density coatings from particles impinging at high velocities. Accordingly, the SoDs were extended whereat a sufficient time in the hot plume and thereby a distinct fraction of melting during flight should be still obtained. Although the deposition efficiencies were acceptable and the degree of crystallinity (DoC) was promising, a decline in deposition efficiency and an increasing surface roughness had to be accepted. This was an indication that particles indeed were already cooling down from maximum temperature and molten fractions tend to re-solidify at the stage of impact. Additionally, (depending on the substrate material used) the particles of high kinetic energy tended to cause erosion on the substrate which could be compensated however reducing the kinetic energy by decreasing the particle size. Nevertheless, this promoted the degree of melting, that is, a lowered DoC, and thus created a dilemma which cannot be solved by adapting the particle size only.

In the current study, a substantially reduced SoD (~1/3 compared to Bakan et al.) was applied so that heating and acceleration of the particles could be expected to be at an early stage and to be on relatively low level. According to the previous studies a critical degree of melting must be achieved to allow for acceptable deposition efficiency and density. At that short SoD, the gas velocity might need to be reduced to keep the residence in the flame sufficient for heat absorption that ensures particles are molten at least superficially. This can also be advantageous in terms of the particle's kinetic energy to prevent erosion of the substrates surface.

The total gas feed to the torch and the oxy-fuel ratio were varied over a wide range applying a full factorial 3×3 experimental plan in order to be able to vary the gas temperature and the gas velocity independently. Furthermore, the characteristics of the expanding gas jet were calculated using a simple one-dimensional flow model and assuming chemical equilibrium. This enables for a mechanism-based interpretation of the test results, especially as the determination of in-flight particle characteristics was not successful since the measured infrared radiation was too weak due to the low particle temperatures. At the end, the coatings were characterized in terms of crystallinity and microstructure.

2 | EXPERIMENTAL PROCEDURE

2.1 | Manufacture of coatings

Monolithic SiC with a porosity of approx. 5% was used as substrate material (CoorsTek GmbH, Mönchengladbach, Germany). These substrates were produced from SiC powder which is isostatically pressed and then sintered at about 2100°C for 24 h. Individual specimens of dimensions $25 \times 25 \times 4$ mm^3 were produced by sawing and grit blasted with SiC particles of size F150 before coating. Substrate roughness R_a was in the order of 4 µm to 5 µm determined by laser scanning confocal microscope VK-X3000 (Keyence) using cut-off wavelengths of $\lambda_S = 2.5$ µm and $\lambda_C = 0.8$ mm.

The HVOF process was carried out in a Multicoat facility equipped with a DJ2700 torch (Oerlikon Metco). Commercial ytterbium disilicate powder (Oerlikon Metco) at particle sizes of $d_{50} = 41$ µm and $d_{50} = 27$ µm, respectively, was used as feedstock. Stand-off distances of 100, 350, and 425 mm, were used, respectively. Mixtures of oxygen and methane were used with normalized oxy-fuel ratios of approximately 0.75, 1, and 1.25 at total feed rates of $0.3 \cdot Q_{HVOF}$, $0.45 \cdot Q_{HVOF}$, and $0.6 \cdot Q_{HVOF}$, respectively. Q_{HVOF} is a reference value that is proprietary. Other parameters were similar to those used in the study by Bakan et al.[9] At the SoD of 100 mm, a three-level full factorial experimental design was executed using

the coarse feedstock. The maximum substrate temperature during deposition was measured by a pyrometer working in the long wavelength infrared range (LWIR). The weight of specimens was taken prior and after coating to determine of the deposition efficiency.

The particle characteristics during flight were tried to investigate using the systems DPV-2000 (TECNAR Automation Ltd.) and Accuraspray-g3 (TECNAR Automation Ltd.). Both systems detect the thermal radiation of the particles to determine their temperature and velocity. However, the measured signals were too weak for evaluation, suggesting rather cold conditions and/or small particles. For this reason, the thermodynamic properties of the working gas have been calculated in order to estimate the effect of parameter variations on the process conditions.

2.2 | Calculation of working gas characteristics

In high-kinetic spray processes like HVOF, the working gas velocity at the critical nozzle cross section cannot exceed the local speed of sound (Mach number $Ma = 1$). The jet becomes supersonic ($Ma > 1$) when subsequently expanding. This can happen in a divergent expansion section of the nozzle. However, in this work on HVOF with O_2+CH_4, the nozzle was cylindrical so that there was no divergent part. Hence, the exit cross-section was regarded as critical cross-section. If the jet is supersonic, that is, the flow in the free jet is at least as fast as the pressure waves traveling in the jet at the local speed of sound, no information on the ambient pressure can be transferred inside the nozzle. This means that the working gas can exit the nozzle at a pressure which is different from the ambient pressure. In all conditions investigated in this study, the jet at the nozzle exit was above the ambient pressure. Thus, it was underexpanded. Such an underexpanded jet tends to enlarge immediately after exiting the nozzle to accommodate with the ambient atmospheric pressure.

More details of the following calculation principles for the working gas composition and properties as well as the torch gas dynamics can be found elsewhere.[14]

2.2.1 | Working gas composition and properties

Working gas composition and properties were calculated using the CEA2 code.[15,16] The thermodynamic states were characterized by assigning specific enthalpy and pressure. The calculation principle to find the chemical equilibrium conditions was the minimization of the Gibbs energy. This was performed by an iterative procedure. Basic assumptions were:

- ideal gas law is applicable,
- instantaneous chemical equilibrium of the gas constituents,
- homogeneous mixing.

Besides the gas composition, the results include the density, specific enthalpy (if not assigned), specific entropy, molar mass, isentropic exponent, specific heat, and the velocity of sound.

2.2.2 | Gas dynamics in the torch

To calculate the gas dynamics inside the torch, the theoretical rocket performance feature of the CEA2 code was used.[15,16] An infinite combustion chamber model is applied where the chamber is assumed to contain a large reservoir of working gas with a particular composition at a given pressure p_{inf}. This pressure had to be adjusted to achieve the actual mass flow of gases through the torch nozzle.

Initially, the temperature and equilibrium compositions in the working gas reservoir were obtained according to Section Working Gas Composition and Properties assigning p_{inf}. The calculation of the nozzle throat conditions (denoted by the subscript t) was then based on the following assumptions, in addition to those mentioned in Section Working Gas Composition and Properties:

- one-dimensional form of the continuity, energy, and momentum equations,
- zero velocity at the infinite working gas reservoir,
- adiabatic conditions,
- isentropic expansion in the nozzle.

Based on the isentropic assumption ($s_{inf} = s_t$), throat conditions were determined iteratively.

Moreover, the pressure in the expanded jet can be given. In this work, this was the atmospheric pressure to consider the state where pressure equilibrium between jet and ambient atmosphere was reached.

2.3 | Coating characterization

X-ray diffractograms (XRD) of powders and coatings were recorded in the range $2\theta = 10°–80°$ with a D4 Endeavour (Bruker AXS GmbH). This diffractometer operates with Cu-K_α radiation ($\lambda = 1.54187$ Å). Data were evaluated with the program HighScore Plus (PANalytical B.V, Almelo, Netherlands). Phase fractions and crystallinity were determined with by Rietveld analysis using TOPAS V4 (Bruker AXS). The degree of crystallinity (DoC) was defined by the ratio of integrated intensities of crystalline phases versus the intensities of all Rietveld pattern including the amorphous hump at about $2\theta = 30°$ according to Madsen et al.[17]

To investigate the microstructure, the specimens were embedded in epoxy resin, cut with a diamond blade saw, and then ground and polished. Images acquired with a Phenom ProX scanning electron microscopes (SEM) (Thermofischer Scientific Inc.) in BSE mode were used to determine the pore fraction in the coatings by means of image analysis using a threshold method (imageJ software, https://imagej.nih.gov/ij/). For each specimen five SEM images of magnifications ×1000 to ×3000 with a size of 2048 × 2048 pixels each were used. The threshold analysis was performed on five randomly chosen image areas of about 1000 pixel edge dimension per SEM image. Regions with through thickness segmentation cracks were excluded from the evaluation.

3 | RESULTS AND DISCUSSION

3.1 | Properties of the working gas and impact on the interaction with particles

3.1.1 | Composition

The calculated values of the gas species' fractions were very similar for all investigated total gas feeds to the torch. The compositions show that the reactions are completed when the gas exits the torch. This is only natural as chemical equilibrium is a basic assumption. For all investigated conditions, CH_4 is completely dissociated. If the oxy-fuel ratio is increased, more carbon is oxidized to CO_2 and less CO is formed. At the same time, the amount of non-oxidized hydrogen decreases and the content of unburned O_2 growths.

Table 1 gives the corresponding calculated average molar masses of the working gas mixtures as function of the normalized oxy-fuel ratio λ; the case of a total gas feed to the torch of $0.45 \cdot Q_{HVOF}$ is given as an example. A clear shift to higher molar weight with increasing oxy-fuel ratio λ was observed as the total number of moles in the combustion gas is smaller due to the more complete reaction. In contrast, the total pressure of the combustion gas only had minor influence.

3.1.2 | Temperature

The calculated working gas temperatures are given in Figure 1A,B as functions of the normalized oxy-fuel ratio for different total gas feeds to the torch. It was already mentioned that these results were obtained by a simplified adiabatic model without considering any enthalpy losses, for example, due to the torch cooling or heat transfer to the ambience. As can be seen from the working gas compositions, the combustion was incomplete and more CO and less CO_2 was generated at $\lambda = 0.75$ compared to higher oxy-fuel ratios. Thus, the combustion enthalpy was lower. Vice versa, less carbon was available for oxidation at $\lambda = 1.25$ compared to lower oxy-fuel ratios leading to lower combustion enthalpies as well. Superposing both effects resulted in maximum temperatures for the stoichiometric case at $\lambda = 1.0$. If the oxy-fuel ratio would have been varied in smaller steps and interdiffusion with the ambient air would have been included, the maximum flame temperature could have been found slightly shifted to the fuel-rich side ($\lambda < 1.0$).[18]

Comparing the working gas temperatures at the nozzle exit (Figure 1A) and in the expanded jet (Figure 1B), the dependence on the total gas flow was converse. On the one hand, the highest temperatures at the nozzle exit were found for the highest total gas feed to the torch; on the other hand, the temperatures were the lowest for this case in the expanded jet. The reason is that at the nozzle exit, the pressures were generally higher than atmospheric; here, the highest pressures were found for the largest total gas feed to the torch (see Table 2). The pressures were very similar for the different oxy-fuel ratios at each of the investigated total gas feeds to the torch.

As mentioned already, the pressure at nozzle exit was the highest in case of the largest total gas feed to the torch. Thus, the pressure dropped and chemical equilibrium was shifted most during expansion to atmospheric pressure in that case. This led to a lower specific inner energy $u \sim T/M$ where T is the temperature and M the molar mass. While the molar mass of the combustion gas changed only slightly if the total gas feed to the torch was varied, the effect was mainly on the temperature. Its drop was largest for the highest total gas feed to the torch.

TABLE 1 Calculated average molar masses of the working gas mixtures as function of the normalized oxy-fuel ratio for the total gas feed of $0.45 \cdot Q_{HVOF}$ to the torch

	$\lambda = 0.75$	$\lambda = 1.0$	$\lambda = 1.25$
Nozzle exit	19.8 g/mol	22.2 g/mol	23.8 g/mol
Expanded jet (0.1 MPa)	20.2 g/mol	22.7 g/mol	24.3 g/mol

3.1.3 | Enthalpy

The calculated mass specific enthalpies of the working gas in expanded condition are given in Figure 1C as functions of the normalized oxy-fuel ratio for different total gas feeds to the torch. At the nozzle exit, they are identical for each investigated oxy-fuel ratio. This is because chemical equilibrium and thus a completed reaction was assumed and the enthalpies are related to the mass of the reactants. Expanding the jet to atmospheric pressure of 0.1 MPa led to a pressure drop from the nozzle exit. By this, the chemical equilibrium was shifted. As discussed above, this lowered the specific inner energy u as a part of the specific enthalpy $h = u + p/\rho$, where p is the pressure and ρ is the density. Moreover, the release of mass specific volume change work p/ρ also contributed to

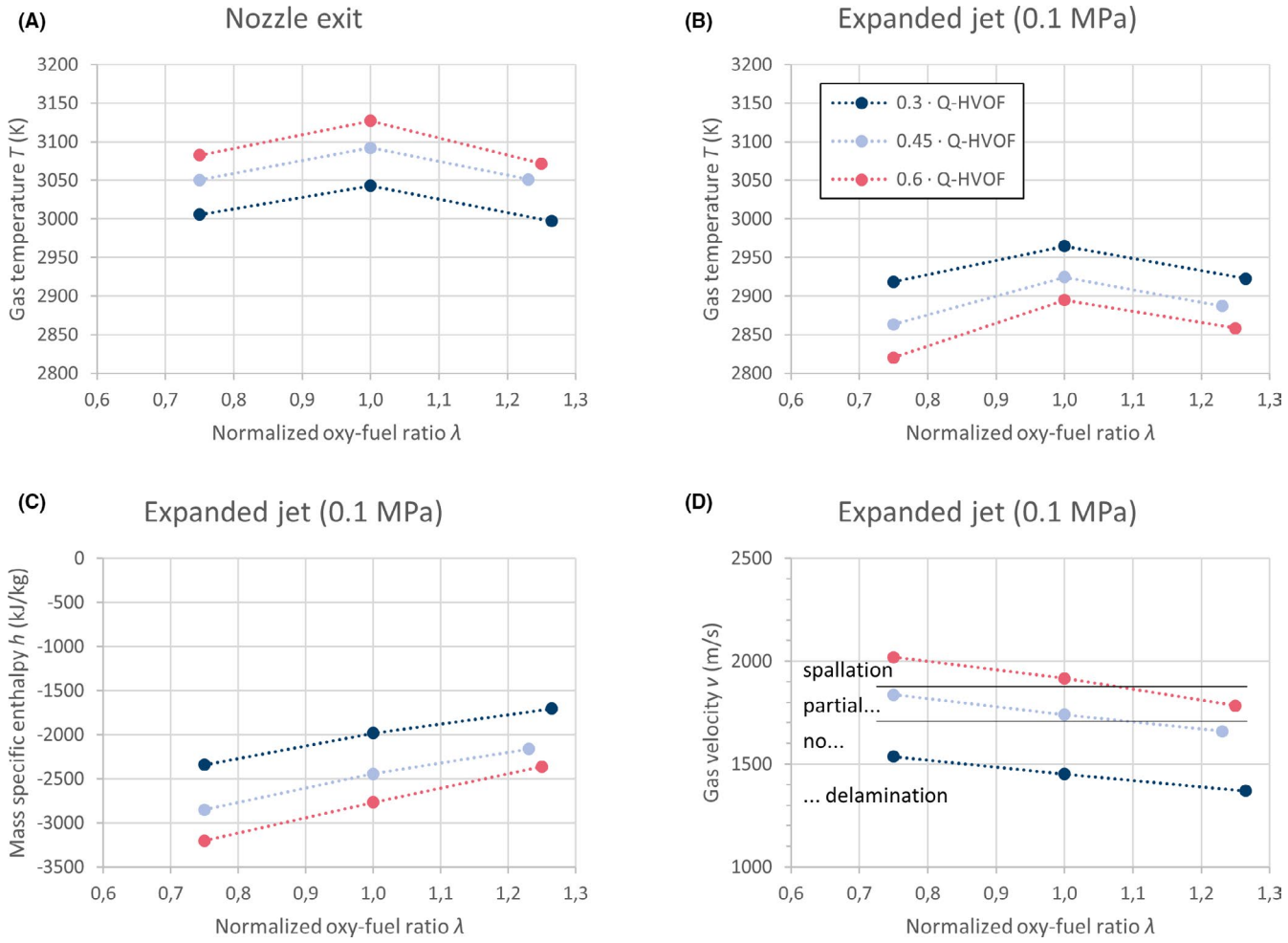

FIGURE 1 Calculated A) + B) working gas temperatures, C) mass specific enthalpies, and D) working gas flow velocities as functions of the normalized oxy-fuel ratio for different total gas feeds to the torch

TABLE 2 Calculated pressures of the working gas as function of the total gas feed to the torch for the normalized oxy-fuel ratio of $\lambda = 1.0$ (*pressure assigned)

	$0.3 \cdot Q_{HVOF}$	$0.45 \cdot Q_{HVOF}$	$0.6 \cdot Q_{HVOF}$
Nozzle exit	0.145 MPa	0.218 MPa	0.292 MPa
Expanded jet*	0.1 MPa	0.1 MPa	0.1 MPa

the enthalpy drop, however to a smaller extent. The pressure at the nozzle exit was highest in the case of the largest total gas feed to the torch (see Table 2). Thus, the pressure drop during jet expansion to atmospheric pressure was the highest. Accordingly, the enthalpy was affected in the same way.

3.1.4 | Velocity

Since the cylindrical nozzle exit was regarded as the critical cross-section, the velocity could not exceed the sonic velocity here, that is, the Mach number equals unity. For ideal gases, the sonic velocity c equals $(\gamma S \bullet p/\rho)^{1/2}$. Since the isentropic exponents γ_S and the pressure-density ratios p/ρ were very similar for each investigated oxy-fuel ratio, the sonic velocities c were comparable.

Since the pressures at the nozzle exit were the highest in case of the largest total gas feed to the torch, the jet was accelerated most and showed the highest velocities (see Table 2). Figure 1D gives the calculated working gas flow velocities as functions of the normalized oxy-fuel ratio for different total gas feeds to the torch. It must be noted that these velocities were calculated by means of the simple one-dimensional adiabatic model as mentioned above. Thus, the results represent an upper estimate of the true flow velocities.

The overall velocity drop at increasing oxy-fuel ratios was related to the gas composition since at higher oxy-fuel ratios, the combustion gas mixtures exhibited higher average molar masses (see Table 1). As the condition for continuity holds for the mass flow, the number of moles passing through the

TABLE 3 Qualitative effects of process parameters on temperature and velocity of the working gas jet and of particle characteristics.

Process parameter	Gas jet			Particle	
(with increase of …)	Velocity (expanded)	Temperature (nozzle exit)	Temperature (expanded)	Velocity	Temperature
Total feed rate	↗	↗	↘	↗	----
Oxy-fuel ratio	↘	/↘	/↘	↘	/↘

TABLE 4 Listing of process parameters and deposition efficiencies, degrees of crystallization, and phase compositions ([§]additional silicon phase identified)

Experiment	Total gas feed rate	Oxy-fuel ratio	Stand-off distance	Particle size, d_{50}	Deposition efficiency	Degree of crystallinity	YbDS	YbMS
	($x \cdot Q_{HVOF}$)	(1)	(mm)	(µm)	(%)	(%)	(%)	(%)
#1	0.3	0.75	100	41	29	93	87	13
#2	0.3	1	100	41	39	92	88	12
#3	0.3	1.25	100	41	36	93	88	12
#4	0.45	0.75	100	41	(45)	92	87	13
#5	0.45	1	100	41	43	92	87	13
#6	0.45	1.25	100	41	48	92	88	12
#7	0.6	0.75	100	41	(17)	n.a.	n.a.	n.a.
#8	0.6	1	100	41	(37)	92	85	15
#9	0.6	1.25	100	41	(47)	95	90	10
#10	0.45	0.75	100	27	11	95	90	1[§]
#11	0.45	0.75	425	41	n.a.	n.a.	n.a.	n.a.
#12	0.45	0.75	425	27	35	26	95	4
#13	0.45	0.75	350	27	41	25	95	4

nozzle was lower than at low oxy-fuel ratios. This implied lower specific volumes and thus lower flow velocities.

3.1.5 | Particle acceleration and heat transfer

The calculation of accurate values for the velocity and heat transfer to the particles requires the integration of the exchange with the stationary gas flow over the entire trajectory and, for example, also the consideration of losses by radiative heat transfer. Nevertheless, also with some simplified assumptions, useful considerations of the expected trends of particle properties can be made.

The transfer coefficient important for the acceleration of particles is the dynamic viscosity μ. Assuming small Reynolds numbers and thus pure Stokesian motion, the acceleration a_p of the feedstock particle is given by $a_p = 6\pi \cdot r_p \cdot \mu \cdot v_r / m_p$, with m_p and r_p the mass and the radius of the particle, respectively, and v_r the relative velocity between the gas jet and the particles.

The calculated variations of μ were very small for the investigated conditions as it ranged from 0.98 to 1.04×10^{-4} Pa•s at the nozzle exit and from 0.94 and $1.0 \bullet 10^{-4}$ Pa•s in the expanded jet. Thus, for a given particle size, the acceleration of particles is proportional to the relative velocity of the gas jet. Particle acceleration is high at small stand-off distances, where the particle velocities are considerably smaller than the gas jet. At the very early stage, neglecting the velocity of the particle, acceleration may practically be considered proportional to the velocity of the gas jet. With increasing distance, particle acceleration decreases until $v_r = 0$ and the drag force turns to deceleration.

The convective heat flow from the working gas to the feedstock particles is proportional to the particle surface area, the temperature difference between working gas and particle surface, and the convective heat transfer coefficient α. For a given particle size and the simplest approach for the Nusselt number $Nu = 2$ for heat transfer between a fluid and a spherical particle, α is directly proportional to the thermal conductivity k of the working gas.

The thermal conductivity of gases depends on the mass and the collision diameter of the gas particles as well as on the temperature. Under the investigated conditions, the largest variations were due to the temperature. Thus, the

development of the thermal conductivity showed the same qualitative characteristics with maxima at $\lambda = 1.0$ while the total gas feed to the torch determined the level of temperatures (see Figure 1A,B)). The overall variation of k was moderate as it ranged from 1.97 to 2.56 W/(m•K) at the nozzle exit and from 1.55 to 2.50 W/(m•K) in the expanded jet.

Another important effect of the total feed rate on the integral heat transfer to the particles was exerted by the particle velocity: the lower the total gas feed rate the higher was not only the temperature of the expanded jet but also the time of flight and thus the amount of energy transferred to the particles.

Considering these dependencies of temperatures and velocities of the expanding jet on the total gas feed rate and oxy-fuel ratio as well as the discussed effect of jet properties on the heating and acceleration of particles, the trends as summarized in Table 3 can be expected. On the one hand, it is evident that the velocity of the particles can be adjusted by the antagonistic effect of total gas feed rate to the torch and the oxy-fuel ratio. On the other hand, the non-monotonic impact of the oxy-fuel ratio and the converse trend of the gas temperatures with the total feed rate at the nozzle exit and in expanded condition does hardly allow for a straight forward control of the particle temperatures, that is, the potential degree of melting.

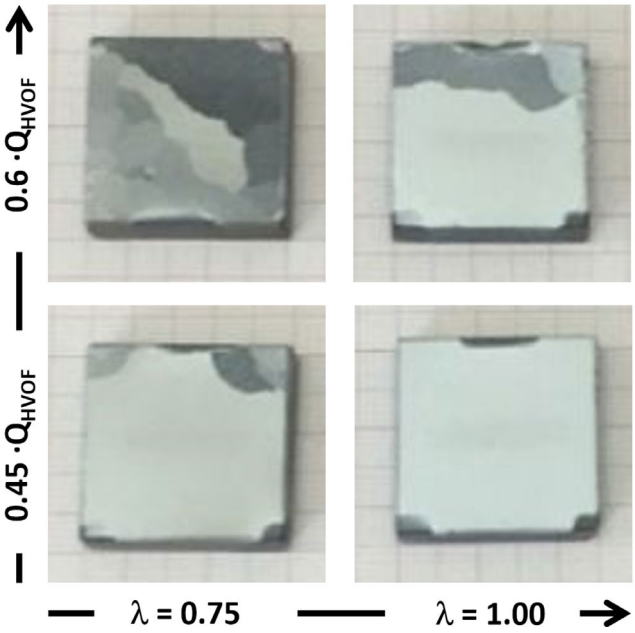

FIGURE 2 Photographs of partially spalled coatings manufactured at high total feed rate and low oxy-fuel ratio in experiments at short stand-off distance using the coarse powder feedstock (experiments #4, #5, #7, and #8)

3.2 | Coating formation and microstructure

3.2.1 | Adhesion and crystallinity

In most of the experiments a continuous coating formation was achieved. The deposition efficiency as determined from weight gain of specimen as well as the degree of crystallinity and the phase composition as determined from Rietveld analysis of the XRD pattern are summarized in Table 4 for coatings obtained at various spray parameters. In cases where the reliable determination of the area specific weight gain or of XRD pattern was prevented due to partial spallation and macroscopic delamination of the coatings, the data in the table is in parentheses "()" or designated as "n.a.".

Considering the results from the DOE carried out at a stand-off distance of 100 mm (experiment #1-#9), the degree of crystallinity of all coatings is impressively high at more than 90%. In case of coatings made from the coarse powder at the short stand-off distance the ratio of YbDS vs. YbMS is virtually unaltered (within the error bandwidth) compared to the feedstock powder. In case of the experiments using the fine powder fraction melting and occasional decomposition of the powder is indicated by the observation of secondary or amorphous phases (experiment #10, #12, #13). The unaltered composition and absence of secondary or amorphous phases in case of the experiments from the DOE strongly suggest that the coarse particles got molten during flight only to a very small extent. Even though prior studies concluded that a sufficient degree of melting is required for high deposition efficiencies, the deposition efficiency is found mostly in the acceptable range of 30–50%. Unfortunately, no clear trend of the deposition efficiency depending on the spraying parameters can be derived. This may be partly attributed to problems in exact determination of the area specific weight gain where parts of the coatings spalled off. Nevertheless, this may also indicate that the impact of process parameters varied in the DOE on the deposition efficiency, even though this is suggested to be linked to the degree of melting, is minor.

Nevertheless, most obvious partial spallation and macroscopic delamination of the coatings observed during deposition and subsequent cool down was found at conditions of high gas feed to the torch and low oxy-fuel ratio (see Figure 2). This is, based on the calculations of gas properties, where high particle velocities can be expected and, as far as the impact of the oxy-fuel ratio is concerned, relatively low particle temperatures. Indeed, the severity of spallation apparently is correlated to the gas velocity of the expanded jet (compare velocity ranges indicated by lines in Figure 1D) which determines to a great extent the velocity and kinetic energy of the impinging particles.

It is interesting to note that in the DOE with the coarse feedstock powder at short stand-off distance delamination and spallation occurred only close to the substrate interface in sharply defined parts of the coating area (experiments #4,

#7-#9, see Figure 2). This changed to a sluggish but homogeneous coating build-up without macroscopic spallation in the experiments where the particle size was reduced or the stand-off distance was considerably increased (experiments #10-#11). This can be attributed to a reduced kinetic energy of particles compared the corresponding experiments of the DOE as the smaller particles carry less mass and the coarse particles decelerate faster at longer distances, respectively. Using the small particle size at an extended stand-off distance (experiment #12-#13) resulted in the formation of mainly amorphous coatings from well molten splats as reported by Bakan et al.[9] This contrasts to the experiments with the coarse powder, on the one hand, again suggests that a high kinetic energy of particles may be an effective parameter to achieve a good adhesion of particles at low degree of melting. On the other hand, it is known from literature that the particles at high kinetic energy may cause erosion of the substrate or of previously deposited coating layers. In the end, this raises the question on the nature of the adhesion mechanism between the splats as well as the stress state in the layers. This is where a closer look into the microstructure of coatings may help.

3.2.2 | Microstructure

The evaluation of the cross sections of the coatings manufactured in the DOE carried out using the coarse powder feedstock at a stand-off distance of 100 mm (experiment #1-#9) showed that not only macroscopic spallation but also macro cracks, segmentation cracks, and localized delamination occurred. Their frequency and extent followed the same distinct trend with the total gas feed rate and the oxy-fuel ratio as the gas velocity: the higher the gas feed rate and the lower the oxy-fuel ratio the higher the frequency and severity of cracking (see ranges indicated by lines in Figure 1D).

Figure 3 shows SEM images of the microstructures at an intermediate magnification of ×2000. It is obvious that inclusion of unmelted particle fragments are regularly observed within the coating layers. Some of those inclusions are exemplarily highlighted by arrows. A higher magnification image of the inclusion marked by the orange frame line is shown in Figure 4. The observation of those inclusions fits well with the observed high degree of crystallinity which was mainly attributed to unmelted fractions of feedstock material. Porosity values obtained by digital image analysis are shown in Figure 5 as function of various process parameters. Number and size of inclusions from unmelted particles are apparently reduced with reduced porosity indicating that those inclusions significantly contribute to the overall porosity.

Taking into account the conclusions drawn on heat transfer in the previous section (see Table 3), that the total heat uptake of particles and thereby the degree of melting will be at its maximum where the velocity of the expanding jet is low and its temperature is high, lowest porosity can be expected at conditions of low total gas feed rate and intermediate oxy-fuel

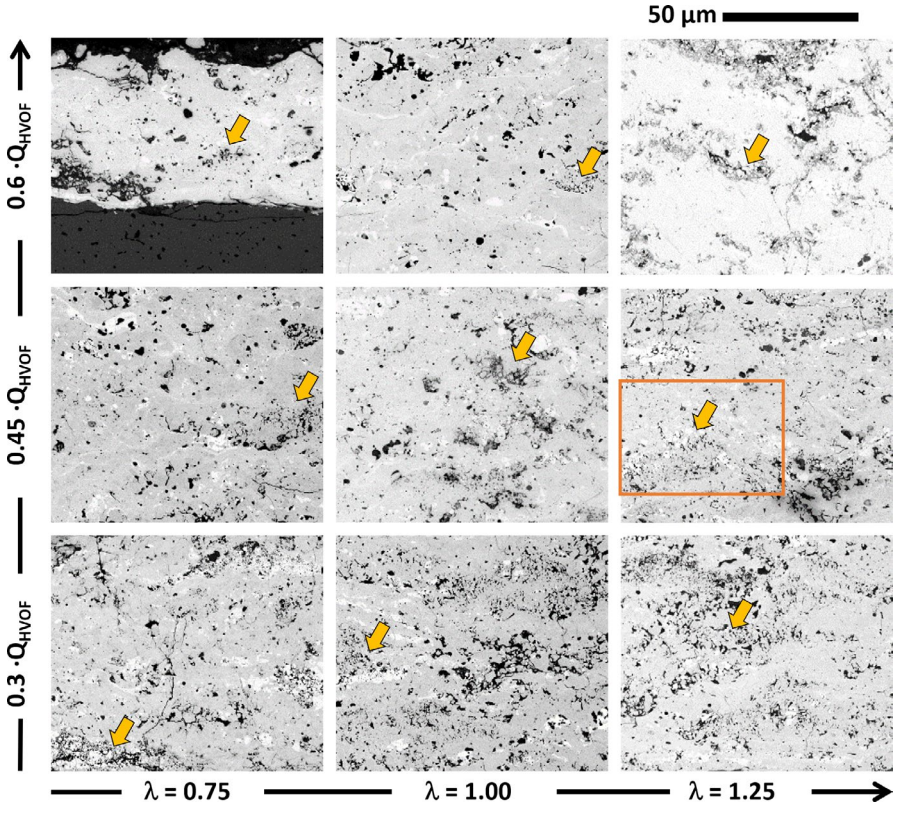

FIGURE 3 SEM images of coatings manufactured in the DOE carried out using the coarse powder feedstock at a stand-off distance of 100 mm (experiment #1-#9). Some inclusions of unmelted particles are exemplarily highlighted by arrows. The region marked by the orange frame is also shown in Figure 4

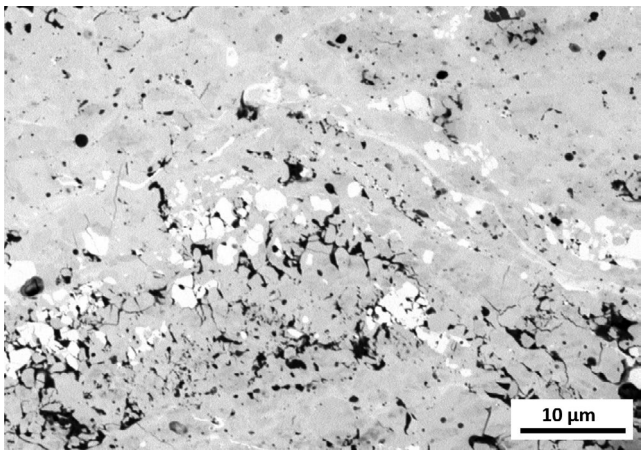

FIGURE 4 Inclusion of unmelted particles in the microstructure of coating from experiment #6 (also marked by an orange frame in Figure 3)

ratio. Indeed, the lowest porosity is observed where the highest gas velocities are obtained due to the high total feed rate while gas temperatures of the expanded jet are not at a maximum due to reduced oxy-fuel ratio (shown in Figure 5A,B). This is apparently in contrast to the conclusion reported in literature that manufacture of dense ceramic coatings mainly relies on the distinct melting of feedstock particles in flight. Nevertheless, the general trend of decreasing porosity with increasing gas temperature at the nozzle exit (shown in Figure 5C) still may indicate that this temperature better describes the heat uptake at the short stand-off distance. Obviously, the fraction of molten material is at a sufficient level.

The almost linear dependency of the porosity on the jet velocity once more supports the conclusion that the kinetic energy of the particles exerts the dominating effect on the compaction of the coatings at this short stand-off distance. In this context it is also interesting to note, that the lower

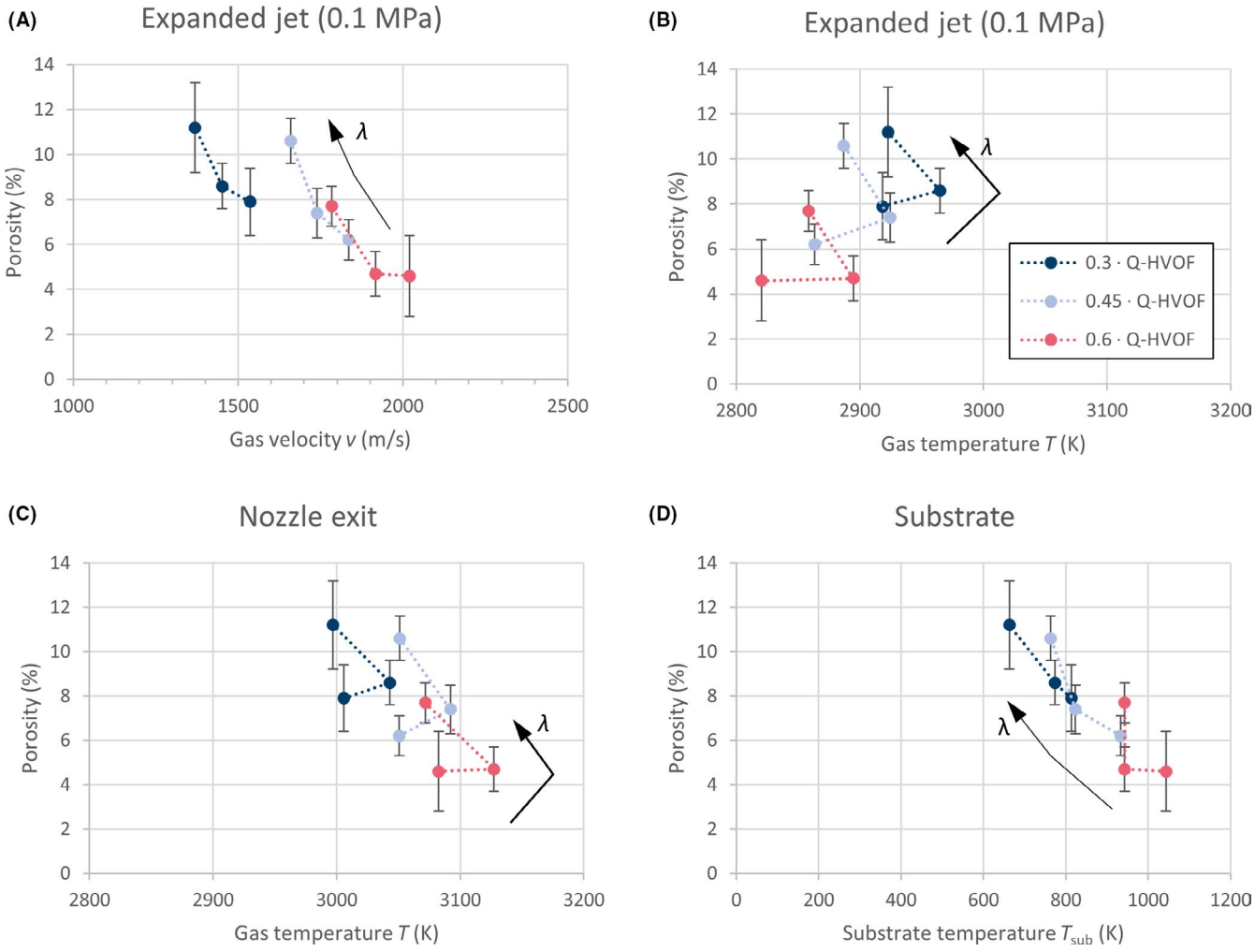

FIGURE 5 Porosity of the coatings as determined by image analysis depending on (A) the velocity of the expanded gas jet, (B) the temperature of the expanded gas jet, (C) the temperature of the gas jet at nozzle exit, and (D) the substrate temperature during deposition for different normalized oxy-fuel ratios and different total gas feeds to the torch

porosity in these experiments also correlates with higher substrate temperatures (see Figure 5D). The substrate temperatures up to 1040 K observed at the short stand-off distances where distinctively higher compared to temperatures in the order of 500 K observed in the experiments carried out with extended stand-off distance (experiment #11-#13). As the ductility of material generally increases with temperature, this can be interpreted in the way that the formation of dense coatings is facilitated by (relatively) ductile initial coatings layers which can be (further) compacted by peening with (relatively) fast and rigid particles. This suggested mechanism is also in-line with the coincidence of compaction and cracking of the coatings: The released kinetic energy was not fully converted to ductile deformation but also introduces stresses in the layer already deposited. Pfeiffer et al.[19, 20] showed in their work that these stresses in ceramic coatings can reach a depth of 100 µm in the layer. Therefore, it can be assumed that the stresses continue to build up with each pass of deposition and are eventually relaxed by crack initiation. This effect is amplified by the fact that the strain tolerance of the layers progressively decreases with decreasing porosity.[21, 22] This corresponds well to the observation of macroscopic spallation at conditions where highest particle velocity and lowest coating porosity coincide (Figure 5A).

4 | SUMMARY AND OUTLOOK

In this study, YbDS coatings with a degree of crystallinity above 90%, porosities below 10%, and low amounts of cracks were manufactured by HVOF spraying at short stand-off distance. An experimental series varying the total feed and the oxy-fuel ratio of the working gas was carried out to better understand the effect of particle temperatures and velocities to coating formation.

While the formation of dense coatings and the occurrence of cracks in thermally sprayed YbDS often can be correlated to the fraction of molten material and recrystallization from the amorphous state, these effects only play a minor role in this work. Instead, the level of porosity and the cohesion of the coatings was found mainly dependent on the kinetic energy of the particles and also on the ductility and strain tolerance of the substrate. Dense and crystalline coatings were assumed to build up from particles of low melting degree if the kinetic energy of particles and the ductility of the substrate layer is sufficiently high to allow for compaction. This must be substantiated in future work. Nevertheless, it remains undecided yet whether the kinetic energy of particles or the limited strain tolerance of the compacted coatings must be considered more to prevent cracking and spallation of the coatings: for the 40 µm particles processed in this work, it appears as if porosities of less than ~7% could not be achieved as the impact of particles exceeding a specific velocity threshold was found to cause critical stresses in the coating.

A further step towards dense and predominantly crystalline YbDS coatings should be possible by introducing surface modifications on the substrates to improve the adhesion of the initial coating layer and prevent spallation. Alternatively, a slight shift to process conditions with an increased heat transfer may effect a more quasi-ductile behavior of impinging particles while keeping the level of molten fraction below a critical level. Those kinds of conditions will be accessible by using agglomerated nano-scaled feedstock but also by technologies as high velocity atmospheric plasma spraying.

ACKNOWLEDGEMENT

The authors thank F. Kurze, R. Laufs, K.-H. Rauwald, and M. Kappertz (all IEK-1, Forschungszentrum Jülich) for performing thermal spraying and supporting in materialographic preparations. The authors also thank Dr. Y.-J. Sohn (IEK-1, Forschungszentrum Jülich) for performing the Rietveld analyses and Dr. E. Bakan for fruitful discussions.

CONFLICT OF INTEREST

The authors declare no conflict of interest.

ORCID

Markus Wolf https://orcid.org/0000-0003-2217-7563
Daniel Emil Mack https://orcid.org/0000-0002-0365-4582
Georg Mauer https://orcid.org/0000-0002-0840-8006
Olivier Guillon https://orcid.org/0000-0003-4831-5725
Robert Vaßen https://orcid.org/0000-0002-9198-3991

REFERENCES

1. Bansal NP. Handbook of ceramic composites. Boston, MA: Kluwer; 2005.
2. Bansal NP, Lamon J. Ceramic matrix composites: materials, modeling and technology. Hoboken, NJ: Wiley; 2014.
3. Gupta AK, Lilley DG. Combustion and environmental challenges for gas turbines in the 1990s. J Propul Power. 1994;10(2):137–47.
4. Jacobson NS, Fox DS, Smialek JL, Opila EJ, Tortorelli PF, More KL, et al. Corrosion issues for ceramics in gas turbines. In: Roode MV, Ferber MK and Richerson DW editor. Ceramic gas turbine component development and characterization. New York, NY: ASME Press; 2003. p. 607–40.
5. Lee KN. Current status of environmental barrier coatings for Si-Based ceramics. Surf Coat Technol. 2000;133–134:1–7.
6. Bakan E, Mack DE, Mauer G, Vaßen R, Lamon J, Padture NP. 1 - High-temperature materials for power generation in gas turbines. In: Guillon O, editors. Advanced ceramics for energy conversion and storage. Amsterdam, the Netherlands: Elsevier; 2020. p. 3–62.
7. Lee KN, Miller RA, Jacobson NS. New generation of plasma-sprayed mullite coatings on silicon carbide. J Am Ceram Soc. 1995;78(3):705–10.

8. Bakan E, Marcano D, Zhou D, Sohn YJ, Mauer G, Vaßen R. $Yb_2Si_2O_7$ environmental barrier coatings deposited by various thermal spray techniques: a preliminary comparative study. J Therm Spray Techn. 2017;26(6):1011–24.
9. Bakan E, Mauer G, Sohn Y, Koch D, Vaßen R. Application of High-Velocity Oxygen-Fuel (HVOF) spraying to the fabrication of Yb-silicate environmental barrier coatings. Coatings. 2017;7(4):55.
10. Bolelli G, Lusvarghi L, Manfredini T, Mantini FP, Polini R, Turunen E, et al. Comparison between plasma- and HVOF-sprayed ceramic coatings. Part I: microstructure and mechanical properties. Int J Surf Sci Eng. 2007;1(1):38–61.
11. Hasan S, Stokes J. Design of experiment analysis of the Sulzer Metco DJ high velocity oxy-fuel coating of hydroxyapatite for orthopedic applications. J Therm Spray Techn. 2011;20(1):186–94.
12. Kulkarni A, Gutleber J, Sampath S, Goland A, Lindquist WB, Herman H, et al. Studies of the microstructure and properties of dense ceramic coatings produced by high-velocity oxygen-fuel combustion spraying. Mater Sci Eng, A. 2004;369(1):124–37.
13. Varis T, Knuuttila J, Turunen E, Leivo J, Silvonen J, Oksa M. Improved protection properties by using nanostructured ceramic powders for HVOF coatings. J Therm Spray Techn. 2007;16(4):524–32.
14. Mauer G. Plasma characteristics and plasma-feedstock interaction under PS-PVD process conditions. Plasma Chem Plasma Process. 2014;34(5):1171–86.
15. Gordon S, McBride BJ. Computer Program for Calculation of Complex Chemical Equilibrium Compositions and Applications - Analysis. NASA-Reference Publication, 1311 part 1. Cleveland, OH: NASA Lewis Research Center; 1994.
16. Gordon S, McBride BJ. Computer Program for Calculation of Complex Chemical Equilibrium Compositions and Applications – User's Manual and Program Description. NASA-Reference Publication 1311, part 2. Cleveland, OH: NASA Lewis Research Center; 1996.
17. Madsen IC, Scarlett NVY, Kern A. Description and survey of methodologies for the determination of amorphous content via X-ray powder diffraction. Z Kristallogr. 2011;226(12):944–55.
18. Cheng D, Xu Q, Tapaga G, Lavernia EJ. A numerical study of high-velocity oxygen fuel thermal spraying process. Part I: gas phase dynamics. Metall and Mat Trans A. 2001;32(7):1609–20.
19. Pfeiffer W, Frey T. Strengthening of ceramics by shot peening. J Eur Ceram Soc. 2006;26(13):2639–45.
20. Pfeiffer W, Wenzel J. Shot Peening Of Brittle Materials - Status And Outlook. Mat Sc Forum. 2010;638–642:799–804.
21. Guo HB, Vaßen R, Stöver D. Atmospheric plasma sprayed thick thermal barrier coatings with high segmentation crack density. Surf Coat Technol. 2004;186(3):353–63.
22. Zhou Z, Shang J, Chen Y, Liang X, Shen B, Zhang Z. Synchronous shot peening applied on HVOF for improvement on wear resistance of Fe-based amorphous coating. Coatings. 2020;10(2):187.

How to cite this article: Wolf M, Mack DE, Mauer G, Guillon O, Vaßen R. Crystalline ytterbium disilicate environmental barrier coatings made by high velocity oxygen fuel spraying. *Int J Appl Ceram Technol*. 2022;19:210–220. https://doi.org/10.1111/ijac.13829